

## B. Chen

Energy Safety Research Institute,  
College of Engineering,  
Swansea University Bay Campus,  
Swansea SA1 8EN, UK;  
Zienkiewicz Centre for Computational  
Engineering, College of Engineering,  
Swansea University Bay Campus,  
Swansea SA1 8EN, UK

## Andrew R. Barron

Energy Safety Research Institute,  
College of Engineering,  
Swansea University Bay Campus,  
Swansea SA1 8EN, UK;  
Department of Chemistry,  
Rice University,  
Houston, TX 77005;  
Department of Materials Science and  
Nanoengineering,  
Rice University,  
Houston, TX 77005

## D. R. J. Owen

Zienkiewicz Centre for Computational  
Engineering,  
College of Engineering,  
Swansea University Bay Campus,  
Swansea SA1 8EN, UK

## Chen-Feng Li

Energy Safety Research Institute,  
College of Engineering,  
Swansea University Bay Campus,  
Swansea SA1 8EN, UK;  
Zienkiewicz Centre for Computational  
Engineering, College of Engineering,  
Swansea University Bay Campus,  
Swansea SA1 8EN, UK;  
Department of Chemistry,  
Rice University,  
Houston, TX 77005;  
Department of Materials Science  
and Nanoengineering,  
Rice University,  
Houston, TX 77005

# Propagation of a Plane Strain Hydraulic Fracture With a Fluid Lag in Permeable Rock

*Based on the KGD scheme, this paper investigates, with both analytical and numerical approaches, the propagation of a hydraulic fracture with a fluid lag in permeable rock. On the analytical aspect, the general form of normalized governing equations is first formulated to take into account both fluid lag and leak-off during the process of hydraulic fracturing. Then a new self-similar solution corresponding to the limiting case of zero dimensionless confining stress ( $\mathcal{T} = 0$ ) and infinite dimensionless leak-off coefficient ( $\mathcal{L} = \infty$ ) is obtained. A dimensionless parameter  $\mathcal{R}$  is proposed to indicate the propagation regimes of hydraulic fracture in more general cases, where  $\mathcal{R}$  is defined as the ratio of the two time-scales related to the dimensionless confining stress  $\mathcal{T}$  and the dimensionless leak-off coefficient  $\mathcal{L}$ . In addition, a robust finite element-based KGD model has been developed to simulate the transient process from  $\mathcal{L} = 0$  to  $\mathcal{L} = \infty$  under  $\mathcal{T} = 0$ , and the numerical solutions converge and agree well with the self-similar solution at  $\mathcal{T} = 0$  and  $\mathcal{L} = \infty$ . More general processes from  $\mathcal{T} = 0$  and  $\mathcal{L} = 0$  to  $\mathcal{T} = \infty$  and  $\mathcal{L} = \infty$  for three different values of  $\mathcal{R}$  are also simulated, which proves the effectiveness of the proposed dimensionless parameter  $\mathcal{R}$  for indicating fracture regimes. [DOI: 10.1115/1.4040331]*

*Keywords:* hydraulic fracture, self-similar solution, fluid lag, leak-off, parametric space

## 1 Introduction

Owing to the increasing adoption in the oil & gas industries, hydraulic fracturing has been extensively researched for nearly half a century, using analytical, experimental, and numerical approaches. An influential set of work is the systematic semi-analytical studies based on the KGD model [1–3], among others. These studies have led to the classification of different kinds of propagation regimes, as well as providing benchmarks for more advanced numerical studies. The KGD model was first developed by Khristianovic and Zheltov [4] and Geertsma and De Klerk [5], and then was improved by Detournay and his coworkers since 1999 [6]. The problem of hydraulic fracturing is significantly simplified with the following assumptions: (1) plane strain assumption and (2) fracture propagation along a straight line. With

respect to governing equations, the elastic equation is used to model the rock deformation while Poiseuille's law and the continuity equation are adopted to simulate the fluid flow. Fracture propagation is controlled by the linear elastic fracture mechanics theory. Despite the strict assumptions, the important characteristics including nonlocal character of elastic response and coupling between fluid flow and rock deformation are captured by the KGD model.

In the pioneering work [7], Spence and Sharp derived a self-similar solution for the KGD model using a scaling approach. The scaling approach was systematically extended by Detournay and his coworkers [8–11] to obtain a series of self-similar solutions at different limiting cases, from which various fracture propagation regimes are uniformly recognized in a clearly structured parametric space, as shown in Fig. 1. The scaling approach transforms the key unknowns including fluid pressure, fracture width and length into time-independent normalized counterparts. In the meantime, the governing equations are also transformed into normalized

Manuscript received February 22, 2018; final manuscript received May 13, 2018; published online June 14, 2018. Editor: Yonggang Huang.

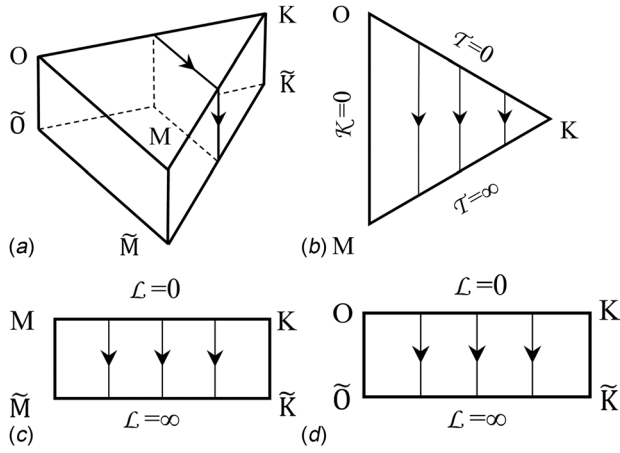


**Fig. 1 Parametric space of plane strain hydraulic fracturing and limiting propagation regimes**

governing equations, which can be solved analytically or numerically [6,7,10–13].

Based on the aforementioned solution strategy, the plane strain propagation of hydraulic fracture has been extensively studied [14]. According to the analytical analysis, the propagation regimes of a hydraulic fracture are mainly determined by three dimensionless parameters, namely the dimensionless toughness  $\mathcal{K}$ , the dimensionless confining stress  $\mathcal{T}$ , and the dimensionless leak-off coefficient  $\mathcal{L}$  [1,2,12]. These three dimensionless parameters ranging from 0 to  $\infty$  are functions of rock and fluid properties, in situ stress conditions, and treatment parameters. A wedge-shaped parametric space, shown in Fig. 1(a), has been constructed considering the merging of early time ( $\mathcal{T} \ll 1$ ) and late time ( $\mathcal{T} \gg 1$ ) solutions for large dimensionless toughness [15]. Different combinations of the values or evolutions of the three dimensionless parameters correspond to different propagation regimes. For example,  $\mathcal{K} = \infty$ ,  $\mathcal{T} = 0$ , and  $\mathcal{L} = 0$  corresponds to toughness-storage-dominated propagation of hydraulic fracture (vertex K). To summarize, the following cases have been investigated semi-analytically: (1) edge MK ( $0 < \mathcal{K} < \infty$ ,  $\mathcal{T} = \infty$  and  $\mathcal{L} = 0$ ) [7]; (2) Vertex M ( $\mathcal{K} = 0$ ,  $\mathcal{T} = \infty$ , and  $\mathcal{L} = 0$ ) [6,10]; (3) Vertex M ( $\mathcal{K} = 1$ ,  $\mathcal{T} = \infty$ , and  $\mathcal{L} = 0$ ) [11]; (4) K  $\tilde{K}$  edge ( $\mathcal{K} = \infty$  and

$0 \leq \mathcal{L} < \infty$ ) [16,17]; (5) Vertex O and K, edge OK ( $0 \leq \mathcal{K} < \infty$ ,  $\mathcal{T} = 0$ , and  $\mathcal{L} = 0$ ) [12]; (6) Vertex K ( $\mathcal{K} \gg 1$  and  $\mathcal{L} = 0$ ) [3,18]; (7) Plane OMK ( $0 < \mathcal{K} < \infty$ ,  $0 < \mathcal{T} < \infty$ , and  $\mathcal{L} = 0$ ) [1]; (8) Vertex M,  $\tilde{M}$  and edge MM ( $\mathcal{K} = 0$ ,  $\mathcal{T} = \infty$ , and  $0 \leq \mathcal{L} < \infty$ ) [2]; and (9) Plane MK  $\tilde{M}\tilde{K}$  ( $0 < \mathcal{K} < \infty$ ,  $\mathcal{T} = \infty$ , and  $0 \leq \mathcal{L} < \infty$ ) [13]. A comprehensive review of these solutions is presented in Ref. [14]. These existing semi-analytical solutions have served as benchmarks for extensive numerical algorithms [19–21]. More recently, Dontsov [22] derived the approximate solutions for all the vertices and edges on MK  $\tilde{M}\tilde{K}$  plane and verified them with numerical solutions. Self-similar solutions with respect to porous media have also attracted increasing attention recently [23,24].

Apart from the analytical investigations, the hydraulic fractures propagating in specific propagation regimes have also been simulated numerically. Desroches and Thiercelin [25] developed a hydraulic fracturing model named Loramec in KGD scheme. By using an integrovariational approach for the elasticity equation, both the fracture width and fluid pressure were expressed and solved on a one-dimensional (1D) mesh. Fluid lag and leak-off have been simulated separately and the corresponding results have been used to verify the semi-analytical solutions [6,9]. Without considering leak-off, Hunsweck et al. [26] developed a finite element-based hydraulic fracturing model following the KGD scheme. The numerical results match well with the self-similar early time and late-time solutions.

However, the previous analytical and numerical solutions all stay on OMK and MK  $\tilde{M}\tilde{K}$  plane (shown in Figs. 1(b) and 1(c)). In this study, the self-similar solutions on  $\tilde{O}\tilde{K}$  edge ( $0 < \mathcal{K} < \infty$ ,  $\mathcal{T} = 0$ , and  $\mathcal{L} = \infty$ ) are obtained with a semi-analytical approach, while the transient solution from OK edge to  $\tilde{O}\tilde{K}$  edge (OK  $\tilde{O}\tilde{K}$  Plane:  $0 < \mathcal{K} < \infty$ ,  $\mathcal{T} = 0$ , and  $0 < \mathcal{T} < \infty$ ), shown in Fig. 1(d), and the transient solution from OK edge to  $\tilde{M}\tilde{K}$  edge are solved numerically. The current study differs from the previous studies in the sense that the fluid lag and leak-off need to be modelled simultaneously, which requires complete governing equations with both fluid lag and leak-off considered in the theoretical analysis and a robust numerical model to deal with related simulation issues due to significant decrease of fluid front velocity caused by leak-off. A new dimensionless parameter is proposed to indicate the propagation regimes of hydraulic fracture in more general cases. The rest of the paper is organized as follows: In Sec. 2, the problem formulation and governing equations are presented. In Sec. 3, the general form of the normalized equations suitable for the analysis of both fluid lag and leak-off is derived first. The asymptotic solutions for hydraulic fracturing under zero dimensionless confining stress and infinite dimensionless leak-off coefficient are solved. A finite element-based KGD model is developed in Sec. 4. The semi-analytical and numerical results for the asymptotic and transient solutions are discussed and compared in Sec. 5.

## 2 Mathematical Models

We base our study on a KGD model as shown in Fig. 2, where a plane strain assumption is applied along the plane orthogonal to the vertical wellbore. The rock formation is assumed to be linear elastic, plane strain, and permeable. To simulate the fracturing fluid, the incompressible Newtonian fluid model is adopted with the laminar-flow assumption. The stress boundary conditions are set according to the confining stresses, while the influence from gravity is ignored as it is orthogonal to the simulation plane. A constant injection flow rate is imposed on the injection point at the center of the model. A strict assumption in the KGD model is that the hydraulic fracture propagates along a straight line. For the sake of completeness, the governing equations for rock deformation, fluid flow, and fracture propagation are briefly summarized below.

Rock deformation is computed according to an elastic singular integral equation that relates the fracture width  $w$  to the net pressure  $p = p_f - \sigma_0$ :

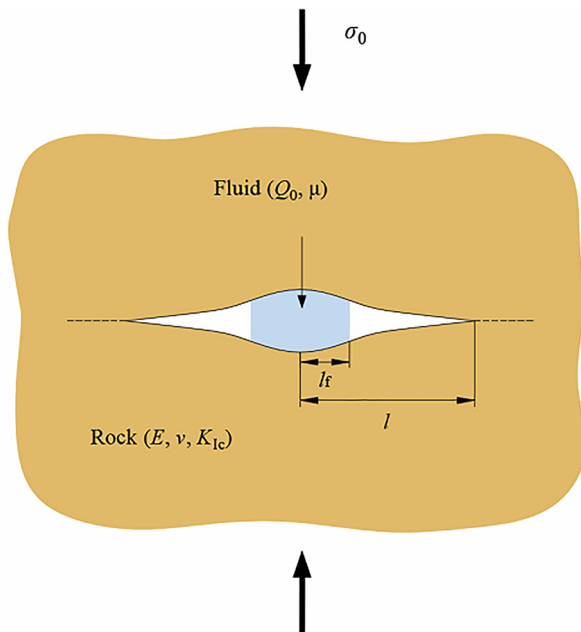


**Fig. 2 Sketch of the KGD model**

$$w = \frac{1}{E'} \int_0^{l_f} G\left(\frac{x}{l}, \frac{s}{l}\right) p ds - \frac{\sigma_0}{E'} \int_{l_f}^l G\left(\frac{x}{l}, \frac{s}{l}\right) ds \quad (1)$$

where  $p_f$  is the fluid pressure,  $\sigma_0$  is the confining stress in the rock formation,  $E' = E/(1 - \nu^2)$  is the plane strain modulus,  $E$  and  $\nu$  are the Young's modulus and Poisson's ratio of the rock, respectively,  $l$  is half length of the fracture,  $l_f$  is half length of fluid channel, and the integral kernel  $G$  is expressed as

$$G(\xi, \eta) = \frac{4}{\pi} \ln \left| \frac{\sqrt{1 - \xi^2} + \sqrt{1 - \eta^2}}{\sqrt{1 - \xi^2} - \sqrt{1 - \eta^2}} \right| \quad (2)$$

As commonly adopted in previous studies [1,12,26], the fluid pressure inside the fluid lag is assumed to be zero. In practice, the speed of fracture propagation in solid rocks is likely to be much higher than the velocity of fluid transport within the fracture, therefore creating a void space near the fracture tip. Pore fluids may find their way into the cavity, but the leaking rate may not keep up with the pace of fracture propagation, especially in the case of dry or tight formations. In these situations, a zero pressure zone is formed at the fluid lag. However, the zero-pressure assumption unlikely holds when the porous medium is highly permeable and saturated.

As the width of a hydraulic fracture is much smaller than the other two dimensions, a lubrication theory, known as the Poiseuille's law (or the cubic law), is commonly adopted to describe the momentum conservation of fracturing fluid

$$q = -\frac{w^3}{\mu'} \frac{\partial p_f}{\partial s} \quad (3)$$

where  $q$  is the flow rate,  $w$  is the fracture width,  $\mu' = 12\mu$ ,  $\mu$  is the viscosity of the fracturing fluid,  $p_f$  is the fluid pressure, and  $s$  is the local coordinate aligned with the tangential direction to the fracture path. Considering the leak-off, the mass conservation for fluid flow is expressed as

$$\frac{\partial w}{\partial t} + \frac{\partial q}{\partial s} + g = 0 \quad (4)$$

where  $\partial t$  denotes time derivative. Leakoff flow rate  $g$  is determined according to Carter's leakoff model

$$g = \frac{C'}{\sqrt{t - t_0(s)}} \quad (5)$$

where  $C' = 2C_L$ ,  $C_L$  is the leak-off coefficient, and  $t_0$  is the time at which the fluid front arrived to a given point of coordinate  $s$ .

Substituting Eqs. (3) into 4 yields

$$\frac{\partial w}{\partial t} - \frac{1}{12\mu} \frac{\partial}{\partial s} \left( w^3 \frac{\partial p_f}{\partial s} \right) + g = 0 \quad (6)$$

The corresponding boundary condition for this equation is a constant injection flow rate  $Q_0$  at  $s = 0$ .

The global continuity equation can be obtained by integrating equation (6) along the fracture length and time

$$\frac{1}{2} Q_0 t = \int_0^{l_f} w ds + 2C' \int_0^{l_f} \sqrt{t - t_0(s)} ds \quad (7)$$

It is assumed that the hydraulic fracture propagates in mobile equilibrium along a straight line which means the mode I stress intensity factor is always equal to the rock toughness  $K_{Ic}$ . The stress intensity factor  $K_I$  is computed by

$$K_I = 2\sqrt{\frac{l}{\pi}} \left( \int_0^{l_f} \frac{p}{\sqrt{l^2 - x^2}} dx + \int_{l_f}^l \frac{-\sigma_0}{\sqrt{l^2 - x^2}} dx \right) \quad (8)$$

### 3 Asymptotic Solutions

**3.1 Normalized Governing Equations.** Since the pioneering work [7–9], scaling has been adopted as an indispensable step in deducing analytical solutions for hydraulic fracturing to transfer the governing equations into dimensionless forms without time emerges. A common form of scaling can be expressed as [3]

$$\begin{aligned} l(t) &= L\gamma \\ p(x, t) &= \varepsilon E' \Pi \\ w(x, t) &= \varepsilon L \Omega \end{aligned} \quad (9)$$

where  $L$  is a length scale,  $\varepsilon$  is a small factor,  $\xi$ ,  $\gamma$ ,  $\Pi$ , and  $\Omega$  are normalized coordinate along fracture, normalized fracture length, normalized net pressure, and normalized fracture width.

Introducing the scaling equation (9) into the governing equations (1) and (6–8) results in a set of normalized governing equations.

- Normalized elastic equation

$$\frac{\Omega}{\gamma} = \int_0^{\xi_f} G(\xi, \xi') \Pi(\xi', t) d\xi' - \mathcal{T} \int_{\xi_f}^1 G(\xi, \xi') d\xi', \quad \xi \in (0, 1) \quad (10)$$

- Normalized Poiseuille's law

$$\begin{aligned} \mathcal{G}_v \left[ \left( \frac{t\dot{\gamma}}{\gamma} + \frac{t\dot{\varepsilon}}{\varepsilon} + 2\frac{t\dot{L}}{L} \right) \int_{\xi}^{\xi_f} \Omega d\xi + \mathfrak{t} \Omega_f \xi_f + \Omega \xi \left( \frac{t\dot{\gamma}}{\gamma} + \frac{t\dot{L}}{L} \right) + \int_{\xi}^{\xi_f} \mathfrak{t} \dot{\Omega} d\xi \right] \\ + \mathcal{G}_c \int_{\xi}^{\xi_f} \Gamma d\xi = -\frac{1}{\mathcal{G}_m} \frac{\Omega^3}{\gamma^2} \frac{\partial \Pi}{\partial \xi}, \quad \xi \in (0, \xi_f) \end{aligned} \quad (11)$$

$\Gamma = 1/\sqrt{1 - \theta(\xi)}$ ,  $\theta(\xi) = t_0/t$  is the normalized arrival time of fluid front remaining to be determined.

The corresponding boundary condition in the lag is

$$\Pi = -\mathcal{T}, \quad \xi \in [\xi_f, 1] \quad (12)$$

- Global continuity equation

$$\frac{1}{2\gamma} = \mathcal{G}_v \int_0^{\xi_f} \Omega d\xi + 2\mathcal{G}_c \int_0^{\xi_f} \sqrt{1 - \theta(\xi)} d\xi \quad (13)$$

- Fracture propagation criterion

$$\mathcal{G}_k = \frac{2^{7/2}}{\pi} \gamma^{1/2} \left( \int_0^{\xi_f} \frac{\Pi d\xi}{\sqrt{1 - \xi^2}} - \mathcal{T} \arccos \xi_f \right) \quad (14)$$

Where  $\mathcal{G}_v = \varepsilon L^2 / Q_0 t$ ,  $\mathcal{G}_c = C' L / Q_0 t^{1/2}$ , and  $\mathcal{G}_m = Q_0 \mu' / \varepsilon^4 L^2 E'$

$$\mathcal{G}_k = \frac{K'}{\varepsilon E' L^{1/2}} \quad \text{and} \quad \mathcal{T} = \frac{\sigma_0}{\varepsilon E'} \quad (15)$$

$\xi_f = l_f/l$  is the fluid fraction, the small factor  $\varepsilon$  and the length scale  $L$  are still to be determined according to the specific propagation regimes to be solved and  $K' = 4\sqrt{2}/\pi K_{Ic}$

**3.2 Propagation Regimes.** Represented by solutions  $\{\Omega, \Pi, \gamma, \xi_f\}$  for Eqs. (10)–(14), the behavior of hydraulic

fracturing differs under different conditions described by the five dimensionless parameters. The dimensionless parameters can be divided into three groups: (1)  $\mathcal{G}_m$  and  $\mathcal{G}_k$ ; (2)  $\mathcal{T}$ ; and (3)  $\mathcal{G}_v$  and  $\mathcal{G}_c$ . The factors  $\mathcal{G}_v$  and  $\mathcal{G}_c$  reflect whether the fluid storage or leak-off dominates the hydraulic fracturing process while the factors  $\mathcal{G}_m$  and  $\mathcal{G}_k$  reflect the energy dissipated on driving viscous fluid and fracturing rock. In order to analyze how the input parameters influence hydraulic fracturing behaviors through dimensionless parameters, explicit expressions of dimensionless parameters need to be determined. Without loss of generality, we restrict  $\mathcal{G}_m = 1$  and  $\mathcal{G}_v = 1$ . After solving the scaling parameters  $L$  and  $\varepsilon$ , the other three dimensionless parameters can be expressed as

$$\mathcal{K} = \mathcal{G}_k = K' \left( \frac{1}{Q_0 E^{1/3} \mu'} \right)^{1/4}, \quad \mathcal{T} = \sigma_0 \left( \frac{t}{E^{1/2} \mu'} \right)^{1/3}, \quad (16)$$

$$\mathcal{L} = \mathcal{G}_c = C' \left( \frac{E t}{\mu' Q_0^3} \right)^{1/6}$$

The three dimensionless parameters ranging from 0 to  $\infty$  constitute a wedge-shaped parametric space, shown in Fig. 1(a). The dimensionless toughness  $\mathcal{K}$  is independent of time while both the dimensionless confining stress  $\mathcal{T}$  and dimensionless leak-off coefficient  $\mathcal{L}$  are dynamic parameters evolving with time. In addition, it is assumed that  $\mathcal{K}$  varies from 0 at OM  $\tilde{O}\tilde{M}$  to  $\infty$  at MK  $\tilde{M}\tilde{K}$ ,  $\mathcal{T}$  increases from 0 at OK  $\tilde{O}\tilde{K}$  to  $\infty$  at MK  $\tilde{M}\tilde{K}$ , and  $\mathcal{L}$  increases from 0 at OMK to  $\infty$  at  $\tilde{O}\tilde{M}\tilde{K}$ . In this case, each hydraulic fracturing process corresponds to a path on a plane parallel to OM  $\tilde{O}\tilde{M}$ , as shown in Fig. 1(a). All the paths evolve from a specific point at OK ( $\mathcal{T} = 0$  and  $\mathcal{L} = 0$ ) to  $\tilde{M}\tilde{K}$  ( $\mathcal{T} = \infty$  and  $\mathcal{L} = \infty$ ) but also vary with each other depending on the relative magnitude of the two time-scale related to  $\mathcal{T}$  and  $\mathcal{L}$ , respectively,

$$\mathcal{R} = \frac{t_1}{t_\sigma} = \frac{\mu' Q_0^3}{E' C'^6} \frac{E'^2 \mu'}{\sigma_0^3} = \left( \frac{\sigma_0 Q_0}{E' C'^2} \right)^3 \quad (17)$$

In the case  $\mathcal{R} \gg 1$ , hydraulic fracturing evolves from OK edge to MK edge first and then to  $\tilde{M}\tilde{K}$  edge. Conversely, it evolves from OK edge to  $\tilde{O}\tilde{K}$  edge and then to  $\tilde{M}\tilde{K}$  edge in case of  $\mathcal{R} \ll 1$ . In more general cases,  $\mathcal{R}$  is slightly over 1 (or below 1), hydraulic fracturing gets closer to MK edge (or  $\tilde{O}\tilde{K}$  edge) first and then evolves to  $\tilde{M}\tilde{K}$  edge. Therefore, each pair of  $\mathcal{K}$  and  $\mathcal{R}$  corresponds to a unique path of hydraulic fracturing, and the state of the hydraulic fracturing (i.e., a point on the path) can be further determined once either  $\mathcal{T}$  or  $\mathcal{L}$  is known.

**3.3 Scaling Schemes.** As shown in Fig. 1(a), there are four limiting propagation regimes: OK edge,  $\tilde{O}\tilde{K}$  edge, MK edge, and  $\tilde{M}\tilde{K}$  edge. The asymptotic solutions at OK edge, MK edge, and  $\tilde{M}\tilde{K}$  edge have been reported in literatures [7,12,13], while the remaining asymptotic solution at  $\tilde{O}\tilde{K}$  edge is obtained in this study. At  $\tilde{O}\tilde{K}$  edge, the propagation of hydraulic fracture is dominated by leak-off, hence  $\mathcal{G}_c = 1$ . For the sake of convenience, the viscosity scaling is chosen here, i.e.,  $\mathcal{G}_m = 1$ . Thus, the scaling parameters can be expressed as

$$\varepsilon = \left( \frac{\mu' C'^2}{E' Q_0 t} \right)^{1/4}, \quad L = \left( \frac{Q_0^2 t}{C'^2} \right)^{1/2} \quad (18)$$

Thus

$$\mathcal{G}_v = \left( \frac{\mu' Q_0^3}{E' C'^6 t} \right)^{1/4}, \quad \mathcal{K} = \mathcal{G}_k = K' \left( \frac{1}{Q_0 E^{1/3} \mu'} \right)^{1/4}, \quad \mathcal{T} = \sigma_0 \left( \frac{t}{E^{1/2} \mu'} \right)^{1/3} \quad (19)$$

For  $\tilde{O}\tilde{K}$  edge,  $\mu' Q_0^3 / E' C'^6 \ll t \ll E'^2 \mu' / \sigma_0^3$ , therefore

$$\mathcal{G}_v = 0, \quad \mathcal{T} = 0 \quad (20)$$

**3.4 Semi-Analytical Solutions.** Substituting  $\mathcal{G}_c = \mathcal{G}_m = 1$  and Eqs. (18) and (20) into the normalized Eqs. (10)–(14) and rescaling the normalized  $\Omega$  and  $\Pi$  using  $\bar{\Omega} = \Omega \gamma^{-3/4}$ ,  $\bar{\Pi} = \Pi \gamma^{1/4}$  to eliminate the normalized fracture length  $\gamma$  in Eqs. (10) and (11) lead to

- Normalized elastic equation

$$\bar{\Omega} = \int_0^{\xi_f} G(\xi, \xi') \bar{\Pi}(\xi', t) d\xi', \quad \xi \in (0, 1) \quad (21)$$

- Normalized Poiseuille's law

$$\int_{\xi}^{\xi_f} \Gamma d\xi = \bar{\Omega}^3 \frac{\partial \bar{\Pi}}{\partial \xi}, \quad \xi \in (0, \xi_f) \quad (22)$$

where  $\Gamma = 1/\sqrt{1 - \theta(\xi)^2}$ , considering  $l \sim t^{1/2}$  and  $x/\xi_f \sim t_0^{1/2}$ ,  $\theta(\xi) = t_0/t = ((x/\xi_f)/l)^2 = (\xi/\xi_f)^2$

Corresponding boundary condition in the lag is

$$\bar{\Pi} = 0, \quad \xi \in [\xi_f, 1] \quad (23)$$

- Global continuity equation

$$\frac{1}{2\gamma} = 2 \int_0^{\xi_f} \sqrt{1 - \theta(\xi)} d\xi \quad (24)$$

- Fracture propagation criterion

$$\mathcal{K} = \frac{2^{7/2}}{\pi} \gamma^{1/2} \int_0^{\xi_f} \frac{\Pi d\xi}{\sqrt{1 - \xi^2}} \quad (25)$$

The self-similar solution  $\{\Omega, \Pi, \gamma, \xi_f\}$  is the function of dimensionless toughness  $\mathcal{K}$  and crack coordinate  $\xi$ . In order to avoid solving the governing equations in a priori unknown domain, Eqs. (21), (22), and (24) are solved first with a given value of  $\xi_f$ . More specifically, the normalized fracture width and fluid pressure are solved using a numerical process detailed in Ref. [12] and the normalized fracture length can be solved explicitly according to Eq. (24). Once the normalized fracture length, fracture width, and fluid pressure are determined, the dimensionless toughness corresponding to these solutions can be computed with Eq. (25). These results are discussed in Sec. 5.

## 4 Numerical model

**4.1 Finite Element Scheme.** The rock deformation is governed by the equilibrium equation and linear elastic constitutive model

$$\nabla \cdot \boldsymbol{\sigma} = 0 \quad (26)$$

$$\boldsymbol{\sigma} = \mathbf{C}:\boldsymbol{\varepsilon} \quad (27)$$

in which  $\boldsymbol{\sigma}$ ,  $\boldsymbol{\varepsilon}$ , and  $\mathbf{C}$  denote the stress, strain, and elastic tensor, respectively. For linear elastic rock formations,  $\mathbf{C}$  is determined by the Poisson's ratio  $\nu$  and the Young's modulus  $E$  of the rock.

The finite element method is adopted to solve the rock deformation. The weak form of the equilibrium equation is

$$\int_{\Lambda} \delta \varepsilon_{ij} c_{ijrs} \varepsilon_{rs} d\Lambda - \int_{\Gamma_e} \delta u_i t_i d\Gamma_e - \int_{\Gamma} \delta u_i p_i d\Gamma = 0 \quad (28)$$

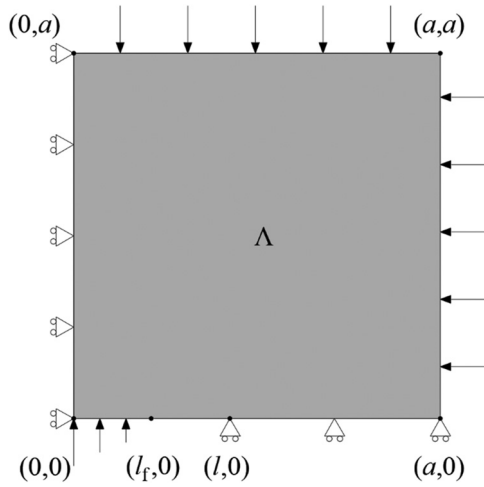


**Fig. 3 Computational model for quarter of the KGD scheme. The injection point locates in the origin.  $(l, 0)$  and  $(l_f, 0)$  are the location of crack tip and fluid front respectively.  $a = 50l$  at the beginning of the simulation and doubles when  $l > a/25$ .**

where  $\Lambda$  is the domain of surrounding medium,  $\Gamma_e$  is the external boundary,  $p$  and  $\Gamma$  are the fluid pressure and the 1D fracture path, respectively.  $\delta \varepsilon_{ij}$  is the strain corresponding to virtual displacement  $\delta u_i$ .

To accurately track the fluid front in relation to the fracture tip and to simplify mesh operations, we take a finite element approach for the fluid solution as well. Specifically, the weak form of Eq. (6) is

$$\int_{\Gamma} \delta p \frac{\partial w}{\partial t} d\Gamma + \int_{\Gamma} (\delta p)_{,s} \frac{w^3}{12\mu} p_{,s} d\Gamma - \delta p(0)q(0) + \delta p(s_f)q(s_f) + \int_{\Gamma} g d\Gamma = 0 \quad (29)$$

where  $p(0)$  and  $q(0)$  are the fluid pressure and the flow rate at the injection point (i.e., fracture center), and  $p(s_f)$  and  $q(s_f)$  are the fluid pressure and the flow rate at the fluid front. A constant injection flow rate  $q(0)$  is assumed at the center of the initial fracture. The pressure at the fluid lag is set to zero, i.e.,  $p(s_f) = 0$ .

**4.2 Spatial and Temporal Discretization.** Following the symmetry of the KGD model, only a quarter of the whole domain is considered, as shown in Fig. 3. At the beginning of the simulation, the finite element simulation domain is set as  $50L_0$  by  $50L_0$  (i.e.,  $a = 50L_0$ ) to approximate the infinite medium, where  $L_0$  is

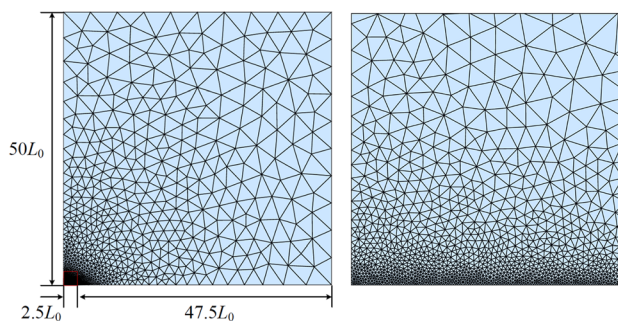


**Fig. 4 Finite element mesh. Left: the entire simulation domain. Right: the mesh in  $(0, 2.5L_0) \times (0, 2.5L_0)$ .**

the initial half-length of fracture and it varies in different numerical cases. The simulation domain is discretized into triangular elements as shown in Fig. 4, where the mesh is refined with a uniform element size in the neighborhood of the fracture (up to  $2.5L_0$  from the center). With a minimum element size of  $L_0/50$  (i.e.,  $a/2500$ ), the number of nodes and triangle elements are 2466 and 4651, respectively. After mesh convergence test, this mesh is used as the initial mesh in all our simulations. During the fracture propagation, the size of the simulation domain is automatically doubled when the fracture length doubles, to keep the fracture stay in the range  $[a/50, a/25]$  and ensure a quality approximation of infinite medium. As the simulation domain grows, the mesh gets updated as well. In most cases, the mesh topology is retained and only the elements are proportionally enlarged.

The fluid front and the fracture tip are both restricted to the element node during simulation. In each time-step, the fluid front is updated first and then the crack tip is updated step by step along the bottom boundary until the fracture criterion is not satisfied. Without remeshing for each fracture advancement, the boundary condition is updated according to the position of fluid front and crack tip. As for the time-step  $\Delta t$ , it is normally determined according to the fluid front velocity explicitly, i.e.,  $\Delta t = d/v_m$  where  $d$  is the advancement limit specified by the user and  $v_m$  is the fluid front velocity at last time-step. However, it is found from our numerical test that the explicit time-step leads to unstable fluid front velocity in the case of very small fluid front advance velocity due to significant leak-off. Here the time-step is determined implicitly using  $\Delta t = 2d/(v_m + v_{m+1})$  where  $v_{m+1}$  is the fluid front velocity at next time-step.  $d$  could be one or several times of the minimum mesh size (3 by default in our simulations). Instead of using an explicit time-step, we update the time-step when solving the elastic equations and fluid flow equation once the preset convergence criteria is met, and the algorithm flow is described in Sec. 4.4.

**4.3 Strongly Coupled Finite Element Solution.** In the following part, a strongly coupled solution process for nodal displacement  $\mathbf{u}_{m+1}$  and the nodal pressure  $\mathbf{p}_{m+1}$  at time  $t_{m+1}$  based on the nodal displacement  $\mathbf{u}_m$  and the nodal pressure  $\mathbf{p}_m$  at time  $t_m$  is explained. At time  $t_{m+1}$ , Eq. (28) can be discretized as

$$\mathbf{K}\mathbf{u}_{m+1} = \mathbf{F}(\mathbf{p}_{m+1}) + \mathbf{F}_{\text{external}} \quad (30)$$

where  $\mathbf{K}$  is the stiffness matrix,  $\mathbf{F}_{\text{external}}$  is nodal force at the domain boundary due to the confining stress of rock formations, and  $\mathbf{F}(\mathbf{p}_{m+1})$  is the nodal force on the fracture due to the fluid pressure, expressed as

$$\mathbf{F}(\mathbf{p}_{m+1}) = \mathbf{T}\mathbf{p}_{m+1} \quad (31)$$

where  $\mathbf{T}$  is a coefficient matrix computed from the 1D fluid mesh. For a linear uniform mesh,  $\mathbf{T}$  has the following form:

$$\mathbf{T} = \sum_e T_{ij}^{(e)}, T_{ij}^{(e)} = \frac{l^e}{6} \begin{bmatrix} 2 & 1 \\ 1 & 2 \end{bmatrix} \quad (32)$$

where  $l^e$  is the element length of the fluid mesh.

Discretizing Eq. (29) with 1D linear finite elements yields

$$\mathbf{L} \cdot (\mathbf{w}_{m+1} - \mathbf{w}_m) / (t_{m+1} - t_m) + \mathbf{h}(\mathbf{w}_{m+1}, \mathbf{p}_{m+1}) + \mathbf{g}(t_{m+1}, \mathbf{t}_0) = \mathbf{q}_{m+1} \quad (33)$$

where  $\mathbf{w}_{m+1}$  and  $\mathbf{w}_m$  are the nodal fracture widths at time  $t_{m+1}$  and  $t_m$ , respectively,  $\mathbf{L}$  is a coefficient matrix,  $\mathbf{h}(\mathbf{w}_{m+1}, \mathbf{p}_{m+1})$  is a non-linear vector function with respect to the nodal fracture width  $\mathbf{w}_{m+1}$  and the nodal fluid pressure  $\mathbf{p}_{m+1}$ ,  $\mathbf{g}(t_{m+1}, \mathbf{t}_0)$  is a vector function with respect to the time  $t_{m+1}$  and the nodal exposed time  $\mathbf{t}_0$ , and  $\mathbf{q}_{m+1}$  is the nodal flow rate at time  $t_{m+1}$ . The fracture path

is discretized into  $N$  linear elements of lengths  $\{l_1, l_2, \dots, l_N\}$  indexed from the crack center to the crack tip, and the first  $N_f$  elements are occupied by the fracturing fluid. The matrix quantities in Eq. (33) are defined as follows:

$$\mathbf{w} = [w_1, w_2, \dots, w_i, \dots, w_{N_f+1}]^T \quad (34a)$$

$$\mathbf{p} = [p_1, p_2, \dots, p_i, \dots, p_{N_f+1}]^T \quad (34b)$$

$$\mathbf{L} = \mathbf{T}(1 : N_f + 1, :) \quad (34c)$$

$$\mathbf{q}_{m+1} = [q(0), 0, \dots, 0, q(N_f + 1)]^T \quad (34d)$$

$$\mathbf{h} = \begin{bmatrix} 0 \\ \hat{\mathbf{h}} \\ 0 \end{bmatrix} \quad (34e)$$

$$\mathbf{g} = \begin{bmatrix} 0 \\ \hat{\mathbf{g}} \\ 0 \end{bmatrix} \quad (34f)$$

where the pressure at the fluid front is set to zero, i.e.,  $p_{N_f+1} = 0$ .  $\hat{\mathbf{h}} = [h_1, h_2, \dots, h_i, \dots, h_{N_f}]^T$  and  $h_i = \frac{1}{48\mu} p_{i+1} - p_i/l_i (w_i^2 + w_{i+1}^2) (w_i + w_{i+1})$ .  $\hat{\mathbf{g}} = [\hat{g}_1, \hat{g}_2, \dots, \hat{g}_i, \dots, \hat{g}_{N_f}]^T$  and  $\tilde{\mathbf{g}} = [\tilde{g}_1, \tilde{g}_2, \dots, \tilde{g}_i, \dots, \tilde{g}_{N_f}]^T$ ,

$$\hat{g}_i = C' l_i \frac{2}{3(\mathbf{t}_0(i) - \mathbf{t}_0(i+1))^2} \left[ (3\mathbf{t}_0(i) - \mathbf{t}_0(i+1) - 2t) \sqrt{t - \mathbf{t}_0(i+1)} + 2(t - \mathbf{t}_0(i))^{3/2} \right] \quad (35a)$$

$$\tilde{g}_i = C' l_i \frac{2}{3(\mathbf{t}_0(i) - \mathbf{t}_0(i+1))^2} \left[ (3\mathbf{t}_0(i+1) - \mathbf{t}_0(i) - 2t) \sqrt{t - \mathbf{t}_0(i)} + 2(t - \mathbf{t}_0(i+1))^{3/2} \right] \quad (35b)$$

Therefore, following a finite element approach, the solid equation (28) and the fluid equation (29) are discretized into finite element equations (30) and (33), respectively, where the nodal fracture width  $\mathbf{w}$  can be directly represented by the nodal displacement  $\mathbf{u}$ . The FE equations (30) and (33) are nonlinear and strongly coupled, and the Newton–Raphson scheme is adopted for their solution:

**Table 1 Dimensionless toughness  $\mathcal{K}$ , fracture length  $\gamma$ , fluid pressure at the inlet  $\Pi(0)$ , and fracture width at the inlet  $\Omega(0)$  under various fluid fraction  $\xi_f$**

$\xi_f$	$\mathcal{K}$	$\gamma$	$\Pi(0)$	$\Omega(0)$
0.001	0.0068	318.31	0.2440	4.6803
0.01	0.0275	31.831	0.3019	0.8019
0.03	0.0554	10.610	0.3425	0.7420
0.1	0.1250	3.1831	0.4060	0.7161
0.2	0.2077	1.5915	0.4582	0.7051
0.3	0.2862	1.0610	0.4977	0.7006
0.4	0.3660	0.7958	0.5318	0.6995
0.5	0.4507	0.6366	0.5631	0.7011
0.6	0.5444	0.5305	0.5931	0.7056
0.7	0.6536	0.4547	0.6232	0.7137
0.8	0.7908	0.3979	0.6547	0.7279
0.9	0.9928	0.3537	0.6914	0.7552
0.97	1.2741	0.3282	0.7296	0.8031
0.99	1.4759	0.3215	0.7524	0.8424
0.999	1.7881	0.3186	0.7875	0.9091

$$\begin{bmatrix} \mathbf{u} \\ \mathbf{p} \end{bmatrix}^{(n+1)} = \begin{bmatrix} \mathbf{u} \\ \mathbf{p} \end{bmatrix}^{(n)} - \mathbf{M}_{\text{Jacobi}} \backslash \mathbf{R} \quad (36)$$

where  $n$  denotes the iteration step,  $\mathbf{M}_{\text{Jacobi}}$  is the Jacobi matrix, and  $\mathbf{R}$  is the residual vector. The Jacobi matrix and the residual vector are given below

$$\mathbf{M}_{\text{Jacobi}} = \begin{bmatrix} \mathbf{K} & -\mathbf{J} \\ \left( \mathbf{L} + \frac{\partial \mathbf{h}}{\partial \mathbf{w}} \right) \frac{\partial \mathbf{w}}{\partial \mathbf{u}} & \frac{\partial \mathbf{h}}{\partial \mathbf{p}} \end{bmatrix} \quad (37a)$$

$$\mathbf{R} = \begin{bmatrix} \mathbf{K}\mathbf{u}^{(n)} - \mathbf{F}(\mathbf{p}^{(n)}) - \mathbf{F}_{\text{external}} \\ \mathbf{L} \cdot (\mathbf{w}^{(n)} - \mathbf{w}_m) / (t_{m+1} - t_m) + \mathbf{h}(\mathbf{w}^{(n)}, \mathbf{p}^{(n)}) - \mathbf{q}_{m+1} \end{bmatrix} \quad (37b)$$

where  $\mathbf{J} = \mathbf{T}(:, 1 : N_f)$ .

**4.4 Algorithm Flow.** For clarity, the overall algorithm flow of the proposed simulation strategy is summarized below:

---

```

Initial condition
Repeat
  Fluid front update
  Repeat
    Crack tip update
    Solving the coupled problem iteratively
    a) Elastic equation and fluid flow equations (Poiseuille's law and
      continuity equation)
    b) Update the time step according to the new fluid front velocity
  Compute the stress intensity factor
  Until fracture criterion is not satisfied
  t ← t+Δt
Until end of simulation

```

---

Initial condition of the numerical simulation is set according to the self-similar solution at OK edge. The stress intensity factor is computed using interaction energy integral method [26–28]. For each crack tip update, the Newton–Raphson scheme is adopted to solve the nonlinear equation system, where the time-step is adaptively adjusted during the iterations.

## 5 Results and Discussion

The semi-analytical and the numerical solution strategies have been described in Secs. 3 and 4, respectively, and the corresponding solutions are presented in this section. In Sec. 5.1, a series of solutions on  $\tilde{\text{OK}}$  edge for different values of dimensionless toughness  $\mathcal{K}$  are obtained. The self-similar solution at  $\mathcal{K} = 0.498$  is verified with the numerical results in Sec. 5.2, in which the transient process from OK edge to  $\tilde{\text{OK}}$  edge is simulated numerically. In Sec. 5.3, the more general processes from OK edge to  $\tilde{\text{MK}}$  edge for three different values of dimensionless parameter  $R$  are simulated, which proves the effectiveness of the proposed dimensionless parameter. The analysis code was implemented with MATLAB and all examples were completed on a PC with an Intel i7-2600 quad-core CPU and 32 GB of RAM.

**5.1 Asymptotic Solution at  $\tilde{\text{OK}}$  Edge.** The self-similar solutions  $\{\Omega, \Pi, \gamma, \xi_f\}$  corresponding to different dimensionless toughness at  $\tilde{\text{OK}}$  edge have been solved from Eqs. (21)–(25) with the methodology explained in Sec. 3.4 and are listed in Table 1. The normalized fracture length is solved explicitly through Eq. (24)

$$\gamma = 1/(\pi \xi_f) \quad (38)$$

Profile of the normalized fracture width and fluid pressure under various value of fluid fraction are shown in Figs. 5 and 6.

**5.2 Approximation of Numerical Solutions to Self-Similar Solution at  $\tilde{OK}$  Edge.** In this case,  $t_\sigma \gg t_1$ , hydraulic fracturing evolves from OK edge to  $\tilde{OK}$  edge first and then to  $\tilde{MK}$  edge. The first stage of the process (shown in Fig. 1(d)) is simulated numerically using the finite element model detailed in Sec. 4. Different values of dimensionless toughness correspond to the different trajectories starting from OK edge and ending at  $\tilde{OK}$  edge. Without loss of generality, we consider the case  $\mathcal{K} = 0.498$ . The initial state of the numerical simulation is set to be the asymptotic solution at OK edge. In order to keep the process in the Plane OK  $\tilde{OK}$ , the confining stress  $\sigma_0$  is set to be zero. The related parameters used in the simulation are listed in Table 2.

The simulation was performed for 205 time-steps, and for each fracture tip update, it took 5–15 Newton–Raphson iterations to solve the coupled displacement and pressure fields. The total simulation time is about 44 min. The half-length of the fracture increases from 1e-2m to 3.9e4m, during which the element size was continuously enlarged as described in Sec. 4.2. The corresponding evolution of the normalized fracture half-length is shown in Fig. 7 and is compared with the limiting propagation regimes at OK edge and  $\tilde{OK}$  edge. In the case  $\mathcal{K} = 0.498$ , evolutions of the fracture half-length in the two different limiting propagation regimes could be expressed as

$$l = L\gamma = \begin{cases} 1.192 \left( \frac{Q_0^3 E' t^4}{\mu'} \right)^{1/6} & \text{OK edge} \\ 0.579 \left( \frac{Q_0^2 t}{C'} \right)^{1/2} & \tilde{OK} \text{ edge} \end{cases} \quad (39)$$

The dimensionless forms of the results are

$$l/l_* = \begin{cases} 1.192(t/t_*)^{2/3} & \text{OK edge} \\ 0.579(t/t_*)^{1/2} & \tilde{OK} \text{ edge} \end{cases} \quad (40)$$

where  $t_* = \mu' Q_0^3 / E' C'^6$ ,  $l_* = (\mu' Q_0^5 / E' C'^8)^{1/2}$

It is indicated from Fig. 7 that fracture length evolves according to the asymptotic solution at OK edge at early-time stage and then approximates to the asymptotic solution at  $\tilde{OK}$  edge with time elapsed. In order to verify the numerical results with the self-similar solutions at  $\tilde{OK}$  edge, the fracture width and fluid pressure

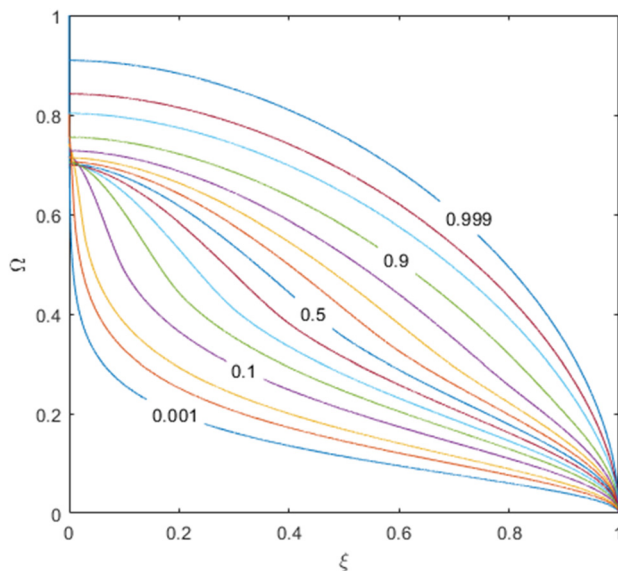


**Fig. 5 Self-similar solutions of normalized fracture width on OK edge for various values of  $\xi_f$  from 0.001 to 0.999 (corresponding values are shown in Table 1)**

solved in numerical simulation are normalized according to Eqs. (9) and (18) and are plotted in Fig. 8. It is shown from Fig. 8 that the normalized fracture width and fluid pressure approximate to the self-similar solution at  $\tilde{OK}$  edge with the time elapsed, which verifies the accuracy of the solutions. During the period, the fluid fraction increases from 0.5 at OK edge to around 0.55 at  $\tilde{OK}$  edge. Although the mobile equilibrium of fracture propagation, i.e.,  $K_I = K_{Ic}$ , is not always exactly satisfied, the error is kept below 2% during the simulation. The accuracy could be improved by using a finer mesh and increasing the step size of fluid front advancement at each time-step.

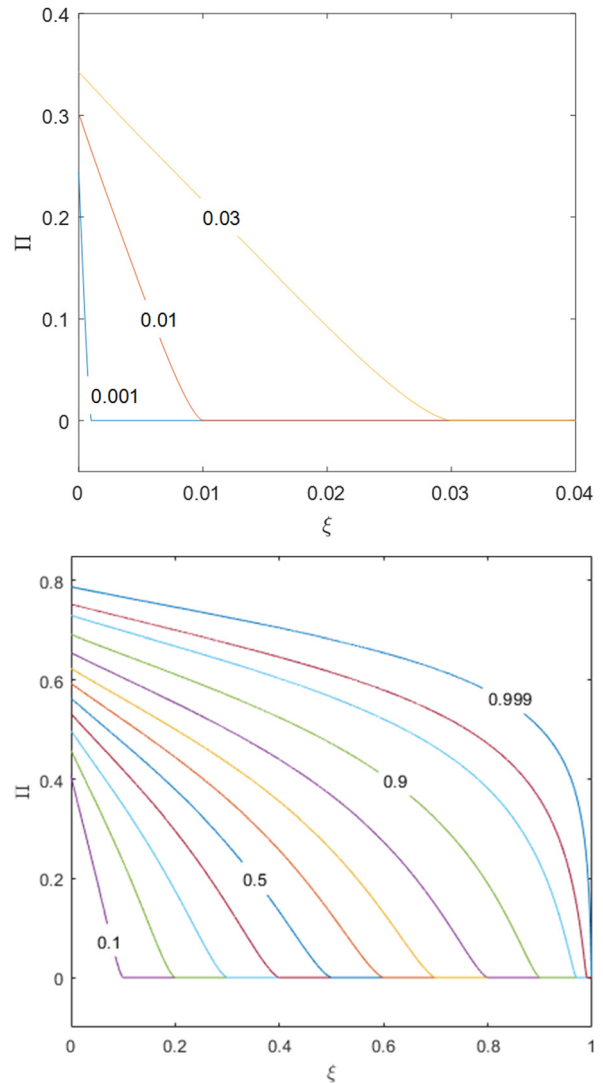


**Fig. 6 Self-similar solutions of normalized fluid pressure on  $\tilde{OK}$  edge for various values of  $\xi_f$  (corresponding values are shown in Table 1). Top: 0.001 to 0.03 and Bottom: 0.1 to 0.999.**

**Table 2 Rock properties, fluid properties, and loading conditions used in numerical simulation**

Elastic modulus	25 GPa
Poisson's ratio	0.3
Toughness	0.876 MPa·m <sup>1/2</sup>
Viscosity	1 cp
Flow rate	0.004 m <sup>2</sup> /s
Confining stress	0 MPa
Leak-off coefficient	1 × 10 <sup>-4</sup> m/s <sup>1/2</sup>

**5.3 Different Propagation Regimes from OK Edge to  $\tilde{M}\tilde{K}$  Edge.** In the case where the relative magnitude of the time-scale  $R \ll 1$  or  $R \gg 1$ , the state of hydraulic fracturing would follow the path from plane OK  $\tilde{O}\tilde{K}$  to plane  $\tilde{O}\tilde{M}\tilde{K}$  or from plane OKM to plane  $\tilde{M}\tilde{K}\tilde{M}$ . In more general case where  $R$  is slightly over or below 1, it would follow a curved path on a plane parallel to plane OM  $\tilde{O}\tilde{M}$  with specific dimensionless toughness. Depending on the relative magnitude of the two time-scales, the path may be close to the line connecting OK edge and  $\tilde{M}\tilde{K}$  edge or bend to  $\tilde{O}\tilde{K}$  edge or MK edge. In the following part, hydraulic fracturing processes with the same dimensionless toughness  $\mathcal{K} = 0.5$  and different  $R$  are simulated with the finite element model detailed in Sec. 4. The related parameters for the numerical cases are listed in Table 3.

For the first case, the simulation was performed for 296 time steps in about 59 min in total, during which it typically took 5–10 iteration steps to solve the coupled displacement and pressure fields. At the beginning, the same mesh (2466 nodes and 4651 triangles) with a minimum element size of  $a/2500$  is used. With the decrease of the fluid lag ratio, a finer mesh is needed. The final mesh has 5501 nodes and 10,443 triangles and the ratio between the minimum mesh size to the side length of the computational domain reduces to  $1/20,000$ . The evolution of the fracture length is shown in Fig. 9 and is compared with the limiting propagation regimes at OK edge and  $\tilde{M}\tilde{K}$  edge. In the case where  $\mathcal{K} = 0.5$ , half-length of the fracture at  $\tilde{M}\tilde{K}$  edge evolves with time as:

$$l = L\gamma = \frac{1}{\pi} \left( \frac{Q_0^2 t}{C\nu^2} \right)^{1/2} \quad (41)$$

Figure 10 plots the hydraulic fracture path in the parametric space. The parametric plane for  $\mathcal{K} = 0.5$  can be defined by  $(\xi_f, r_f)$ , where  $\xi_f$  ranges from 0.5 to 1 and  $r_f$  ranging from 0 to 1 denotes the ratio of fluid volume stored in fracture to the total volume of fluid injected. The four vertices of the domain correspond to the point at which  $\mathcal{K} = 0.5$  on edge OK, MK,  $\tilde{M}\tilde{K}$ , and  $\tilde{O}\tilde{K}$ , respectively, (from (0.5, 1) to (0.5, 0) in clockwise direction). The value of  $R$  is computed as

$$\mathcal{R} = \frac{t_1}{t_\sigma} = \left( \frac{\sigma_0 Q_0}{E' C \nu^2} \right)^3 = 0.0177 \quad (42)$$

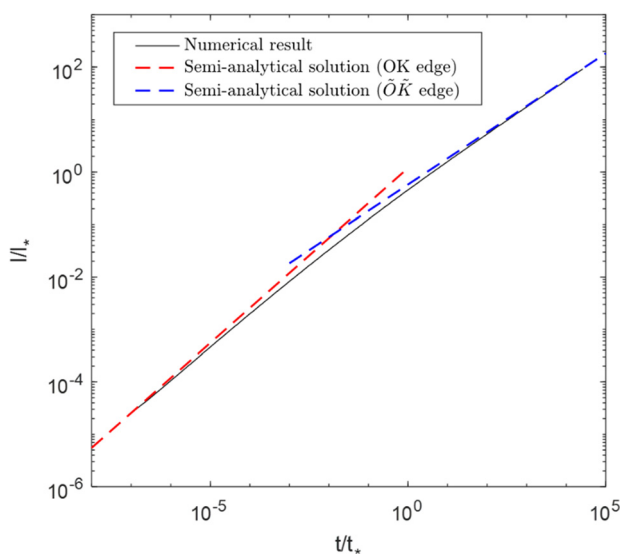


**Fig. 7 Evolution of the normalized fracture half-length with respect to dimensionless time under zero dimensionless confining stress**

As expected, the hydraulic fracturing path evolves from the OK edge at early-time stage to the  $\tilde{M}\tilde{K}$  edge in the end but bends to the  $\tilde{O}\tilde{K}$  edge during the process since  $t_1$  is smaller than  $t_\sigma$ . With the propagation of hydraulic fracture, the fluid fraction approximates to unit. On the aspect of fluid storage, the propagation regime changes from the storage-dominated regime on the top

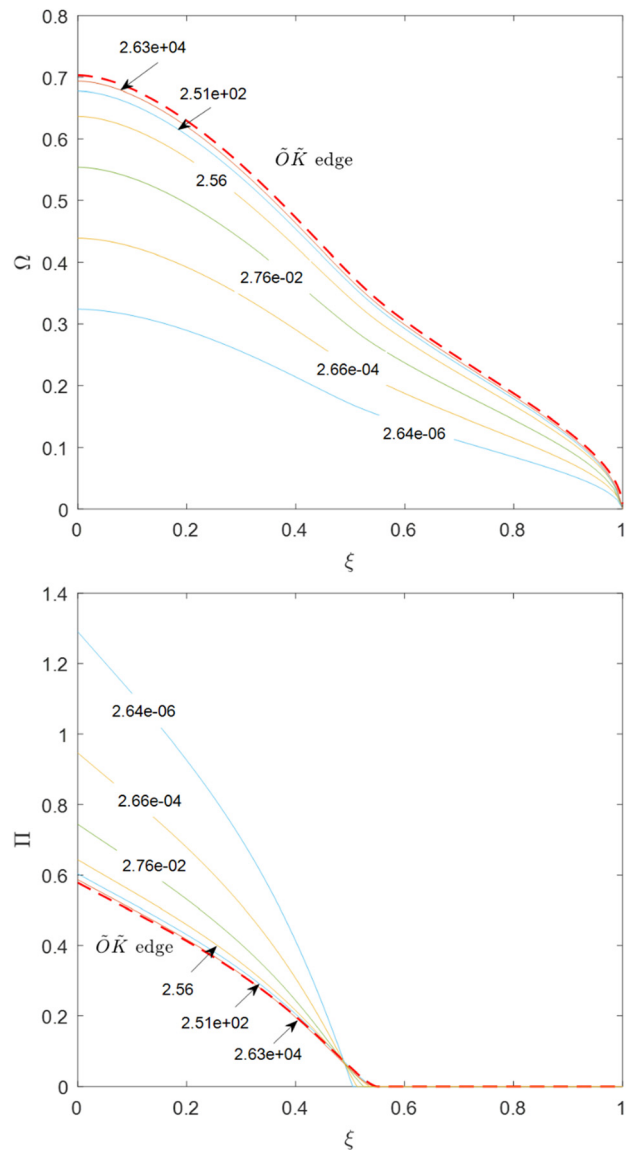


**Fig. 8 Evolution of the normalized fracture width (top) and normalized fluid pressure (bottom) under zero dimensionless confining stress and  $\mathcal{K} = 0.498$ . Solid lines represent the numerical solutions at different dimensionless time  $t/t_1$  and the dashed line represents the self-similar solution at OK edge.**

**Table 3 Rock properties, fluid properties, and loading conditions used in numerical simulation**

Elastic modulus	45 GPa
Poisson's ratio	0.25
Toughness	1.68 MPa·m <sup>1/2</sup>
Viscosity	10 cp
Flow rate	0.00 m <sup>3</sup> /s
Confining stress	50 MPa
Leak-off coefficient	Case 1: $1 \times 10^{-3}$ m/s <sup>1/2</sup> Case 2: $5 \times 10^{-4}$ m/s <sup>1/2</sup> Case 3: $2 \times 10^{-4}$ m/s <sup>1/2</sup>

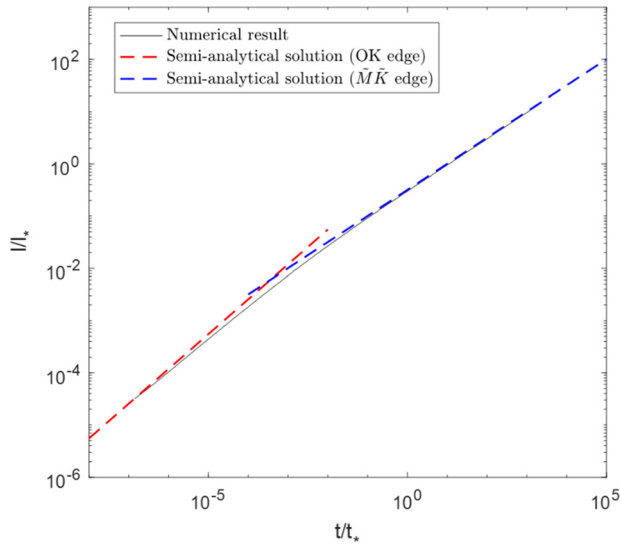


**Fig. 9 Evolution of the fracture half-length with respect to dimensionless time under nonzero dimensionless confining stress**

boundary to the leak-off-dominated regime on the bottom boundary.

In order to check the relation between the dimensionless parameter  $\mathcal{R}$  (i.e., the ratio of the two time-scales) and the corresponding path in the parametric space, another two numerical cases with larger values of  $\mathcal{R}$  are presented. The corresponding paths are compared in Fig. 11. The dimensionless time is not shown due to the slight difference between the correspondence between  $(\xi_f, r_f)$  and  $(t/t_\sigma, t/t_l)$  for different value of  $\mathcal{R}$ .

As shown in Fig. 11, the path for  $\mathcal{R}=1.13$  does not get close to the edge MK and  $\tilde{O}\tilde{K}$  due to the small difference between the two time-scales while the path bends to  $\tilde{O}\tilde{K}$  edge (0.5, 0) for smaller  $\mathcal{R}$  and MK edge (1, 1) for larger  $\mathcal{R}$ , which indicates that the dimensionless parameter  $\mathcal{R}$  has a critical effect on the behavior of hydraulic fracturing.

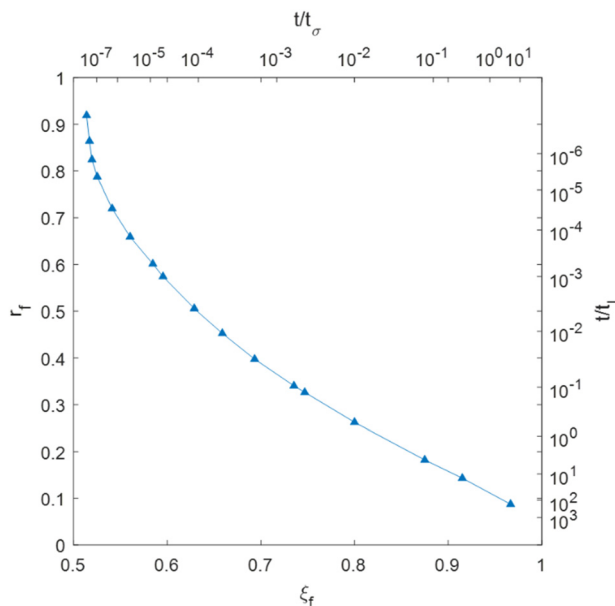


**Fig. 10 Hydraulic fracture path in the case of  $\kappa=0.5$  and  $\mathcal{R}=0.0177$**

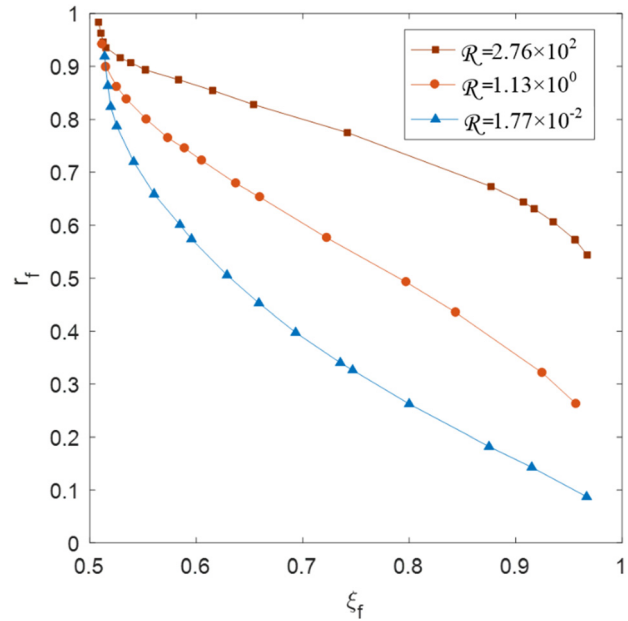


**Fig. 11 Hydraulic fracturing paths in the case of  $\kappa=0.5$  and various value of  $\mathcal{R}$**

## 6 Conclusions

In this paper, the propagation of a hydraulic fracture with a fluid lag in an infinite linear elastic permeable medium is investigated with both analytical and numerical approaches. Based on the KGD scheme, a new self-similar solution of leak-off dominated hydraulic fracturing is solved in a semi-analytical way first. Then, a finite element based model is developed to verify the self-similar solution and to investigate the propagation regimes of hydraulic fracture in more general cases (with both fluid lag and leak-off). The main conclusions of this work are summarized below:

- (1) On the analytical aspect, the general form of normalized governing equations with both fluid lag and leak-off considered is derived firstly. Then the self-similar solution in the limiting case of zero dimensionless confining stress ( $\mathcal{T}=0$ ) and infinite dimensionless leak-off coefficient ( $\mathcal{L}=\infty$ ) ( $\tilde{O}\tilde{K}$  edge in parametric space  $OM\tilde{K}-\tilde{O}\tilde{M}\tilde{K}$ ) is solved in a semi-analytical way while existing analytical and numerical studies only focus on the case with fluid lag or leak-off separately (on  $OM\tilde{K}$  or  $M\tilde{K}$   $\tilde{M}\tilde{K}$  plane). The half-length, fluid net pressure, and fracture width are expressed as,  $l(t) = (Q_0^2 t / C' t^2)^{1/2} \gamma(\mathcal{K})$ ,  $p(x, t) = (\mu' C' t^2 E'^3 / Q_0 t)^{1/4} \Pi(\mathcal{K}, \xi)$  and  $w(x, t) = (\mu' Q_0^3 t / E' C' t^2)^{1/4} \Omega(\mathcal{K}, \xi)$ , respectively. The new self-similar solutions can be regarded as benchmarks for other hydraulic fracture models.
- (2) A new dimensionless parameter  $\mathcal{R}$  is proposed to determine the hydraulic fracturing path in parametric space along with the dimensionless toughness  $\mathcal{K}$ . In the case  $\mathcal{R} \gg 1$ , hydraulic fracturing evolves from OK edge to MK edge firstly and then to  $\tilde{M}\tilde{K}$  edge. Conversely, it evolves from OK edge to  $\tilde{O}\tilde{K}$  edge and then to  $\tilde{M}\tilde{K}$  edge in case of  $\mathcal{R} \ll 1$ . In more general cases,  $\mathcal{R}$  is slightly over 1 (or below 1), hydraulic fracturing paths would only bend to MK edge (or  $\tilde{O}\tilde{K}$  edge) but keep always from them.
- (3) On the numerical aspect, a robust finite element-based KGD model is developed to simulate the propagation of hydraulic fracture with both the fluid lag and leak-off

considered. Both the rock deformation and fluid flow are discretized with finite elements and are solved together using the Newton-Raphson method. The time step in our model is determined implicitly to avoid the fluctuation of fluid front velocity, which makes the program very robust. The transient process from OK edge to  $\tilde{O}\tilde{K}$  edge is simulated and the approximation of the numerical solutions to the self-similar solutions at  $\tilde{O}\tilde{K}$  edge are observed, which verifies the accuracy of the self-similar solution. A more general process from OK edge to  $\tilde{M}\tilde{K}$  edge for various values of  $\mathcal{R}$  is simulated. The effectiveness of the proposed dimensionless parameter  $\mathcal{R}$  is proved. These findings help to understand the various propagation regimes of hydraulic fracture.

## Funding Data

- The authors would like to thank the support from the European Community's Seventh Framework Programme (Marie Curie International Research Staff Exchange Scheme, Grant No. 612607), the Sêr Cymru National Research Network in Advanced Engineering and Materials, the China Scholarship Council, the Welsh Government Sêr Cymru Programme, the Robert A. Welch Foundation (C-0002) and the Royal Academy of Engineering.

## References

- [1] Lecampion, B., and Detournay, E., 2007, "An Implicit Algorithm for the Propagation of a Hydraulic Fracture With a Fluid Lag," *Comput. Methods Appl. Mech. Eng.*, **196**(49–52), pp. 4863–4880.
- [2] Adachi, J. I., and Detournay, E., 2008, "Plane Strain Propagation of a Hydraulic Fracture in a Permeable Rock," *Eng. Fract. Mech.*, **75**(16), pp. 4666–4694.
- [3] Garagash, D. I., 2006, "Plane-Strain Propagation of a Fluid-Driven Fracture During Injection and Shut-in: Asymptotics of Large Toughness," *Eng. Fract. Mech.*, **73**(4), pp. 456–481.
- [4] Khristianovic, S. A., and Zheltov, Y. P., 1955, "Formation of Vertical Fractures by Means of Highly Viscous Liquid," Fourth World Petroleum Congress, Rome, Italy, pp. 579–586.
- [5] Geertsma, J., and De Klerk, F., 1969, "A Rapid Method of Predicting Width and Extent of Hydraulically Induced Fractures," *J. Pet. Technol.*, **21**(12), pp. 1571–1581.
- [6] Carbonell, R., Desroches, J., and Detournay, E., 1999, "A Comparison Between a Semi-Analytical and a Numerical Solution of a Two-Dimensional Hydraulic Fracture," *Int. J. Solids Struct.*, **36**(31–32), pp. 4869–4888.
- [7] Spence, D. A., and Sharp, P., 1985, "Self-Similar Solutions for Elastohydrodynamic Cavity Flow," *Proc. R. Soc. A: Math., Phys. Eng. Sci.*, **400**(1819), pp. 289–313.
- [8] Savitski, A. A., and Detournay, E., 2002, "Propagation of a Penny-Shaped Fluid-Driven Fracture in an Impermeable Rock: Asymptotic Solutions," *Int. J. Solids Struct.*, **39**(26), pp. 6311–6337.
- [9] Detournay, E., 2004, "Propagation Regimes of Fluid-Driven Fractures in Impermeable Rocks," *Int. J. Geomech.*, **4**(1), pp. 35–45.
- [10] Adachi, J. I., and Detournay, E., 2002, "Self-Similar Solution of a Plane-Strain Fracture Driven by a Power-Law Fluid," *Int. J. Numer. Anal. Methods Geomech.*, **26**(6), pp. 579–604.
- [11] Garagash, D. I., and Detournay, E., 2005, "Plane-Strain Propagation of a Fluid-Driven Fracture: Small Toughness Solution," *ASME J. Appl. Mech.*, **72**(6), pp. 916–928.
- [12] Garagash, D. I., 2006, "Propagation of a Plane-Strain Hydraulic Fracture With a Fluid Lag: Early-Time Solution," *Int. J. Solids Struct.*, **43**(18–19), pp. 5811–5835.
- [13] Hu, J., and Garagash, D. I., 2010, "Plane-Strain Propagation of a Fluid-Driven Crack in a Permeable Rock With Fracture Toughness," *J. Eng. Mech.*, **136**(9), pp. 1152–1166.
- [14] Detournay, E., 2016, "Mechanics of Hydraulic Fractures," *Annu. Rev. Fluid Mech.*, **48**(1), pp. 311–339.
- [15] Adachi, J. I., Detournay, E., Garagash, D. I., and Savitski, A. A., 2004, "Interpretation and Design of Hydraulic Fracturing Treatments," U.S. Patent No. US 7111681 B2
- [16] Bungler, A. P., Detournay, E., and Garagash, D. I., 2005, "Toughness-Dominated Hydraulic Fracture With Leak-Off," *Int. J. Fract.*, **134**(2), pp. 175–190.
- [17] Dong, X. L., Zhang, G. Q., Gao, D. L., and Duan, Z. Y., 2017, "Toughness-Dominated Hydraulic Fracture in Permeable Rocks," *ASME J. Appl. Mech.*, **84**(7), p. 071001.
- [18] Garagash, D., 2000, "Hydraulic Fracture Propagation in Elastic Rock With Large Toughness," Fourth North American Rock Mechanics Symposium (ARMA), Seattle, WA, July 31–Aug. 3, pp. 221–228.
- [19] Wang, T., Liu, Z., Zeng, Q., Gao, Y., and Zhuang, Z., 2017, "XFEM Modeling of Hydraulic Fracture in Porous Rocks With Natural Fractures," *Sci. China Phys., Mech. Astron.*, **60**(8), p. 084614.
- [20] Wang, T., Liu, Z., Gao, Y., Zeng, Q., and Zhuang, Z., 2017, "Theoretical and Numerical Models to Predict Fracking Debonding Zone and Optimize Perforation Cluster Spacing in Layered Shale," *ASME J. Appl. Mech.*, **85**(1), p. 011001.
- [21] Zeng, Q., Liu, Z., Wang, T., Gao, Y., and Zhuang, Z., 2017, "Fully Coupled Simulation of Multiple Hydraulic Fractures to Propagate Simultaneously From a Perforated Horizontal Wellbore," *Comput. Mech.*, **61**(1–2), pp. 137–155.
- [22] Dontsov, E. V., 2017, "An Approximate Solution for a Plane Strain Hydraulic Fracture That Accounts for Fracture Toughness, Fluid Viscosity, and Leak-Off," *Int. J. Fract.*, **205**(2), pp. 221–237.
- [23] Detournay, E., Hakobyan, Y., and Eve, R., 2017, "Self-Similar Propagation of a Hydraulic Fracture in a Poroelastic Medium," Biot Conference on Poromechanics, Paris, France, July 9–13, pp. 1909–1914.
- [24] Huynen, A., and Detournay, E., "Self-Similar Propagation of a Plastic Zone Due to Fluid Injection in a Porous Medium," Biot Conference on Poromechanics, Paris, France, July 9–13, pp. 1952–1959.
- [25] Desroches, J., and Thiercelin, M., 1993, "Modelling the Propagation and Closure of Micro-Hydraulic Fractures," *Int. J. Rock Mech. Min. Sci. Geomech. Abstr.*, **30**(7), pp. 1231–1234.
- [26] Hunsweck, M. J., Shen, Y., and Lew, A. J., 2013, "A Finite Element Approach to the Simulation of Hydraulic Fractures With Lag," *Int. J. Numer. Anal. Methods Geomech.*, **37**(9), pp. 993–1015.
- [27] Walters, M. C., Paulino, G. H., and Dodds, R. H., 2005, "Interaction Integral Procedures for 3D Curved Cracks Including Surface Traction," *Eng. Fract. Mech.*, **72**(11), pp. 1635–1663.
- [28] Chen, B., Cen, S., Barron, A. R., Owen, D. R. J., and Li, C., "Numerical Investigation of the Fluid Lag During Hydraulic Fracturing," *Eng. Comput.* (in press).